Investigation into thermal effects in InGaAs/AlAsSb quantum cascade lasers

Craig A. Evans, Vladimir D. Jovanović, Dragan Indjin, Zoran Ikonić, and Paul Harrison
School of Electronic and Electrical Engineering, University of Leeds, Leeds LS2 9JT, United Kingdom

A quantum cascade laser (QCL) thermal model is presented. Based upon a finite-difference approach, the model is used in conjunction with a self-consistent carrier transport model to calculate the temperature distribution in a near-infrared InGaAs/AlAsSb QCL. The presented model is used to investigate the effects of driving conditions and device geometries on the active region temperature, which has a major influence on the device performance. A buried heterostructure (BH) combined with epilayer-down bonding is found to offer the best performance compared to alternative structures and has thermal times constants up to eight times smaller. The presented model provides a valuable tool for understanding the thermal dynamics inside a QCL and will help to improve operating temperatures.

INTRODUCTION

The large threshold currents and voltages in QCLs leading to strong local heating effects in the device active region which can therefore be at a considerably higher temperature than the heat sink. This has serious implications on device performance since the population inversion decreases at higher temperature due to increased levels of electron leakage into continuum-like states and thermal back-filling into the lower laser level. Therefore, in order to achieve the desirable property of room temperature continuous-wave (cw) operation, it is necessary to pay special attention to the device thermal management in order to reduce the active region heating effects.

Several QCLs operating in cw mode at room temperature have been reported using a variety of thermal management techniques. The first report of room temperature cw emission was from a $\lambda \sim 9.1\mu$m InGaAs/AlInAs QCL utilizing a BH configuration mounted epilayer side down on a diamond heat sink [1]. Buried heterostructures offer superior temperature performance compared to standard ridge structures due to the fact that the active region is completely enclosed within the host material (InP in the case of the InGaAs/AlInAs QCL) which allows heat to be dissipated from the active region in all directions compared to standard ridge structures in which the only heat channel is through the substrate. In addition to this, epilayer-down mounting allows the heat generating active region to be in closer proximity to the heat sink thus further improving heat dissipation compared to substrate-side mounted devices.

Although the use of a BH offers superior temperature performance, it comes at the cost of more complicated processing techniques, namely the lateral regrowth of semiconductor material around the active region core. Due to this fact, alternative thermal management techniques have been successfully used to achieve room temperature cw emission. The use of exclusively InP waveguides (due to InP having a higher thermal conductivity than InGaAs) [2] and thick gold layers electroplated on top of the laser ridge to help remove waste heat [3] as well as buried heterostructures [4] and epilayer down mounting [5], has led to several reports of room temperature cw emission in the range $\lambda \sim 4$–6 μm [2–6]. As well as special thermal management techniques, these devices have also utilized strain-balanced InGaAs/AlInAs active regions to increase the temperature performance. The use of strain increases the conduction band offset compared to the lattice-matched system and hence reduces the electron leakage into the continuum-like states at shorter wavelengths. This had led to QCLs operating with high power at room temperature in cw mode (480 mW) and at temperatures as high as 363 K [2]. To date, room temperature QCL cw emission has been limited to to the InP-based material system, not just because of its maturity over GaAs-based QCLs but also due to the high thermal conductivity of InP compared to GaAs meaning that improved temperature performance is inherent to this QCL material system.

Recently InGaAs/AlAsSb QCLs lattice matched to InP substrates have been reported [7]. The InGaAs/AlAsSb heterostructure has a very large conduction band offset of $\sim$1.6 eV which is almost double that of the strained InGaAs/AlInAs heterostructure and makes this material system inherently less sensitive to temperature. These factors led to the rapid development of high temperature InGaAs/AlAsSb QCLs, albeit in pulsed mode. An InGaAs/AlAsSb QCL emitting at $\lambda \sim 4.5\mu$m up to at least 400 K in pulsed mode has been reported [8]. The device was processed into a standard double channel waveguide and mounted substrate side down with no particular attention paid to optimizing the structure to improve the thermal management. Although to date there has been no report of cw emission from InGaAs/AlAsSb QCLs, cw emission has been observed from QCLs in the similar InGaAs/AlGaAsSb material system. Incorporation of Ga into the barrier material reduces the conduction band offset to $\sim$1–1.2 eV, depending on the exact composition of the quarternary layer. This increases the electron tunnelling probability and relaxes the requirement for the growth of ultrathin layers while still providing sufficient quantum confinement for short wavelength emission. Following the report of laser emission from a $\lambda \sim 4.9$ μm InGaAs/AlGaAsSb QCL up to at least 400 K in pulsed mode [9], cw operation up to 94 K from the same active region design was achieved by covering the top and sides of the laser ridge in 2.5 μm thick electroplated gold in order to promote heat removal in the lateral direction [10].

It is clear that the thermal dynamics inside QCL structures must be understood in order to improve the temperature performance. In this work we outline the development of a two dimensional thermal model of a QCL and use it in conjunction with our self-consistent carrier transport calculation [11–13] to investigate the effects of device geometry and drive conditions on the thermal dynamics inside the QCL. The investigation will centre on a $\lambda \sim 3\mu$m InGaAs/AlAsSb QCL, which was the focus of a previously reported simulation [13] of an

experimentally measured device [14].

THEORETICAL BACKGROUND

The electron dynamics inside the device active region were calculated using a self-consistent scattering rate approach [13]. After calculating the electronic states of the QCL, the wavefunctions were then used to evaluate all the principal electron-electron and electron-LO phonon intra- and inter-period scattering rates [15]. The resulting rate equations must be solved self-consistently since the subband populations depend upon both the initial and final populations, and hence the process was repeated until the subband populations converged. The self-consistent solution yields the nonequilibrium electron density and the lifetime of a carrier in each of the subbands, from which the total current density J and the local gain g can be calculated. By repeating the above procedure at different values of electric field strength F and at different lattice temperatures, F–J curves can be generated for each temperature. The self-consistent procedure was run for the $\lambda \sim 3\mu$m InGaAs/AlAsSb QCL and the F–J curves generated for several temperatures. The model gain G_M is calculated using the local gain g and the waveguide parameters (the confinement factor Γ, waveguide losses α_{wg} and mirror losses α_m). The waveguide parameters were calculated using a transfer-matrix technique [16] and in order to include the effect of temperature on the waveguide parameters, a temperature dependent mobility [17] was used to calculate the complex refractive index of the waveguide layers. The calculations show that the InGaAs/AlAsSb QCL has enough gain to achieve laser emission up to a temperature of 300 K.

The thermal model is based upon the heat diffusion equation in two dimensions

$$\rho(x,y,T)c_p(x,y,T)\frac{\partial T(x,y,t)}{\partial t} = \nabla\cdot[\kappa(x,y,T)\nabla T(x,y,t)] + S(x,y,t) \quad (1)$$

where ρ is the density of the material (kg/m^3), c_p is the specific heat capacity of the material (J/kg K), T is the temperature (K), κ is the thermal conductivity (W/m K) and S is the power density of the heat source (W/m^3). Eq. 1 is solved using a finite-difference approach and the temperature cross-section is found explicitly using Euler's forward method. The QCL structure is meshed into a non-overlapping grid which defines the boundaries between the individual control volumes and the temperature is found at the centre (or node) of each of these control volumes (of size $\Delta x = \Delta y = 0.5\mu$m). The two dimensional geometry of the QCL is then mapped onto this grid and the temperature at the centres of each node are calculated in each time step to give a complete time-dependent picture of the thermal dynamics inside a QCL structure. Since QCL experimental measurements are typically made in a vacuated environment, Neumann (zero-derivative - no heat flow) boundary conditions are applied to the surfaces exposed to the vacuum, with a constant temperature boundary condition applied to the surface in contact with the heat sink. The heat source power density S is applied to the device active region and is given by $S = FJ$, with F and J extracted from the generally nonlinear F–J curves mentioned previously. By extracting the values of J at the operating bias point (135 kV/cm) at each temperature, S was calculated as a function of temperature ($= 1000\exp(T/1023)$ GW/m^3). This 'quantum source term' is then inserted into Eq. 1 and succinctly describes the QCL active region heating effects due to dissipative quantum transport processes. We note that the 'quantum source term' is dependent upon the local lattice temperature and is therefore non uniform within the device active region. Both pulsed and cw operating conditions can be simulated by varying the time dependency of S accordingly.

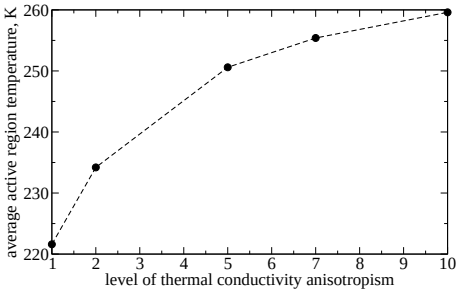

FIG. 1: Average $T_{\rm AR}$ for different levels of anisotropic active region thermal conductivity anisotropism. $T_{\rm sink}$ = 200 K and the pulse width is 100 ns with a 100 kHz repetition rate.

The active region of the QCL is made up from a multitude of thin semiconductor layers and it is impractical to include all the individual layers due to their small dimensions and hence the active region is treated as being just one material. Due to the lack of data for the thermal conductvity of the AlAsSb barriers, the active region is assumed to be purely InGaAs. The thin semiconductor layers create extra phonon scattering channels at the interfaces between these layers [18, 19], and hence the thermal conductivity perpendicular to the layers ($\kappa_\perp$) is found to be approximately an order of magnitude smaller than the thermal conductivity in the plane of the layers ($\kappa_\parallel$) [20]. Fig. 1 shows the effect of the different ratios of $\kappa_\parallel$ to $\kappa_\perp$ on the average active region temperature (T_{AR}) of the InGaAs/AlAsSb QCL at the centre of this work. A heat sink temperature (T_{sink}) of 200 K with 100 ns pulses at a frequency of 100 kHz is used in the simulation. It can be seen from Fig. 1 that with an isotropic thermal conductivity, the average T_{AR} is 222 K and increases with the ratio before starting to saturate at $\kappa_\parallel/\kappa_\perp \approx 10$. Since the ratio is not known exactly, in this work $\kappa_\parallel$ will be taken to be that of bulk InGaAs, and $\kappa_\perp$ a tenth of the bulk value in order to simulate the worst case scenario.

The material parameters are temperature dependent and Table I lists the functional relationships for the material parameters used in the simulations [21–23]. The specific heat capacities are calculated using the Debye specific heat equation

$$c_p = 9N_{AV}k_B\left[\frac{T}{\Theta_D}\right]^3\int_0^{\Theta_D/T}\frac{x^4e^x}{(e^x-1)^2}dx \quad (2)$$

where N_{AV} is Avogadro's number, k_B is the Boltzmann constant and Θ_D is the Debye temperature. The material densities vary only slightly with temperature and are therefore treated as being constant in the simulations.

TABLE I: Material parameters used in the simulations[21–23].

Material	κ [W/m K]	Θ_D [K]	c_p [J/kg K]	ρ [kg/m^3]
InP	[a]	425	-	4.81×10^3
InGaAs	[b]	330	-	5.52×10^3
Au	317	-	128	19.30×10^3
Cu	398	-	385	8.96×10^3
Diamond	2000	-	502	3.52×10^3
In-solder	320	-	233	7.31×10^3
Si_3N_4	10	-	160	3.18×10^3

[a] $406-2T+2.88\times10^{-3}T^2$

[b] $23-9.3\times10^{-2}T+1.06\times10^{-4}T^2$

NUMERICAL RESULTS AND DISCUSSION

Using the thermal model outlined in the previous section, the influence of various aspects of the QCL device design and driving conditions on the temperature performance of the device can be investigated. As discussed earlier, the maximum operating temperature of the $\lambda\sim3\mu$m InGaAs/AlAsSb QCL active region is predicted to be 300 K and the thermal model can be used to find the corresponding T_{sink} for various geometries and driving conditions. In the following sections the QCL active region and waveguide cladding layers are as described in Ref. [13] with the device itself considered to be a standard ridge waveguide of width 10 μm and etched to a depth of 9 μm, mounted substrate side down.

Influence of heat sink temperature

The effect of the heat sink temperature T_{sink} on the active region temperature T_{AR} was investigated using 100 ns pulses at 100 kHz. During pulsed operation, the active region temperature increases rapidly during the pulse and then decays until the next pulse arrives. In the case of high duty cycle operation (high repetition frequency and/or long pulse widths), the active region may not have recovered the heat sink temperature before the next pulse arrives and hence the active region heats up further during the next pulse. This heat accumulation effect gets progressively worse during each subsequent pulse until the device reaches a steady-state. In the following simulations, the active region temperatures are extracted once this steady state has been reached. Also, the temperature distribution within the active region itself is non-uniform and so both the minimum and maximum active region temperature are given. Fig. 2 shows the effect of T_{sink} on T_{AR}. It can be seen from Fig. 2 that both the minimum and maximum T_{AR} increase linearly with T_{sink}. Linear fits of the form $T_{AR}=T_1+\alpha_{s-AR}T_{sink}$, where used to extract the coupling constant between the heat sink and active region, α_{s-AR}. For the case of the minimum T_{AR}, α_{s-AR} = 1.097, while for the maximum T_{AR}, it is equal to 1.167. This shows that the temperature range inside the QCL active region increases with temperature and could cause damaging thermal stress effects at high heat sink temperatures. The cause of the temperature range increase is probably due to the thermal conductivity of the materials in the devices decreasing with temperature. The hotter areas of the active region have a lower thermal conductivity than the cooler areas and are less able to dissipate heat leading to an increase in temperature, while the cooler areas are better able to dissipate heat and hence the temperature rise is not as great. For the case of the InGaAs/AlAsSb QCL at the centre of this work, with 100 ns pulses at 100 kHz (1% duty cycle) and T_{sink} = 220 K, the entirety of the active region is less than 300 K,meaning laser action would be expected for these driving conditions. Above this heat sink temperature, only some of the active region is less than 300 K. Since the temperature gradient inside the active region is in the direction perpendicular to the active region periods, laser action may still occur, but only in those periods at less than 300 K. Above T_{sink} = 260 K, the entirety of the active region is above 300 K and hence this is expected to be the maximum operating temperature of the QCL under the stated driving conditions. The fact that the temperature gradient inside the active region increases with heat sink temperature could help to explain the abrupt decrease in slope efficiency at higher temperatures, just before cut-off which has been measured experimentally [24]. When the device is being operated at close to its maximum temperature, not all of the active region periods may be contributing to laser action. As the heat sink temperature is increased, the temperature gradient is increased further and less periods will contribute to laser action. This process will cause the output power to decrease further (and hence the slope efficiency) until eventually all of the active region periods will cease lasing and the device reaches cut-off. In addition, if each of the active region periods are at a slightly different temperature, the amount of red shift in the emission wavelength will vary, leading to a broadening of the linewidth.

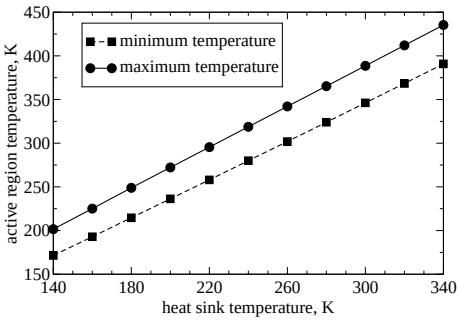

FIG. 2: Spatial minimum and maximum values of T_{AR} for different values of T_{sink} at 100 kHz with 100 ns pulse widths.

Influence of duty cycle

The duty cycle can be increased by increasing either the pulse repetition frequency or the pulse width (or a combination of both). In order to investigate the effect of higher duty cycle operation, the same device as in the previous section was simulated with T_{sink} = 200 K and a pulse width of 100 ns at dif-

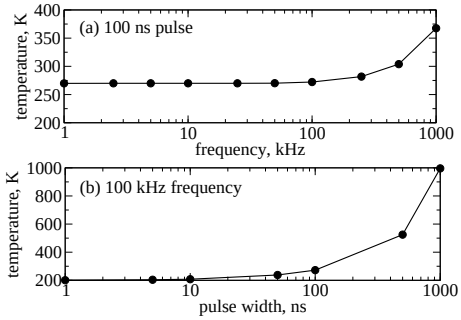

FIG. 3: (a) T_{AR} for different pulse frequencies with a pulse width of 100 ns. (b) T_{AR} for different pulse widths with f = 100 kHz. In both cases T_{sink} = 200 K.

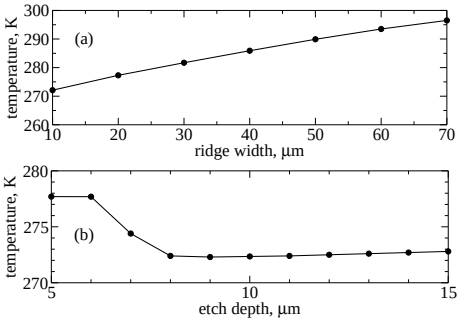

FIG. 4: Maximum values of T_{AR} for (a) different ridge widths and (b) different etch depths.

ferent repetition frequencies and the results are shown in Fig. 3(a). For low frequencies ($<$ 50 kHz), the temperature range of the active region is independent of the pulse frequency. This is due to the relatively long time period between pulses, which gives the active region enough time to entirely dissipate the heat accumulated during the pulse and recover the heat sink temperature. As the frequency is increased beyond this value, heat accumulation effects come into play and the active region temperature begins to rise. With 100 ns pulses and T_{sink} = 200 K, a repetition frequency of $\sim$600 kHz (6 % duty cycle) is possible without the entire active region being above 300 K and hence laser action could occur. The effect of increasing the duty cycle by increasing the pulse width on T_{AR} is shown in Fig. 3(b). For pulse widths of less than 10 ns, very little active region heating occurs. Above this value there is a rapid increase in active region temperature with pulse width. This is due to the same heat accumulation effects as before, but on a more pronounced scale due to the rate of temperature increase during the pulse being far greater than the rate of temperature decrease in between pulses. In Fig. 3(a) for a 100 ns pulse, 1000 kHz corresponds to a 10 % duty cycle and the maximum active region temperature is $\sim$370 K. In the case of Fig. 3(b), a 10 % duty cycle is equivalent to a 1000 ns pulse and the maximum active region temperature is $\sim$ 1000 K. Although this temperature increase is obviously too high and the device would quickly burn out, it shows the effect of having a long pulse width on the active region temperature. In fact, the InGaAs/AlAsSb QCLs which have been reported in the literature have been operated in pulsed mode at extremely low duty cycles of 0.01 ns (100 ns, 1 kHz) in order to avoid large device heating effects.

It can be seen that is better to increase the duty cycle by increasing the pulse repetition frequency rather than increasing the pulse width. In terms of the InGaAs/AlAsSb QCL for a 100 kHz repetition frequency at a 200 K heat sink temperature, a maximum pulse width of $\sim$ 200 ns (2 % duty cycle) is possible without the entire active region temperature rising above 300 K.

Influence of ridge dimensions

The previous sections have investigated the effects of the QCL driving conditions on the active region heating. The thermal model also allows the influence of changing the device structure on the heating effects inside the QCL to be investigated. In this section the effect of the ridge dimensions (width and height) on the active region temperature are investigated. A T_{sink} of 200 K, with 100 ns pulses at 100 kHz is used in the simulations and the results presented in Fig. 4. A constant etch depth of 9 μm is used in Fig. 4(a), and a ridge width of 10 μm used in Fig. 4(b). The results in the Fig. 4(a) agree with experimental measurements [25] in which the active region temperature increases with ridge width. This is an obvious result due to the greater active region volume and hence higher power density and more heating effects. In the case of the QCL in question, ridge widths of at least 70 μm are possible without the active region rising above 300 K. From a thermal standpoint, a narrow ridge would be advantageous, but this would also reduce the maximum power due to the reduced emitting volume and also reduce the mode overlap with the active region, which in turn will reduce the gain. The ridge height is defined by the etch depth and the effect of varying this on the active region temperature range is shown in Fig. 4(b), for the same driving conditions as before. The total thickness of the active region and upper cladding of the InGaAs/AlAsSb QCL is $\sim$7.5 μm, and it can be seen from the figure that once the entirety of the active region is etched through, the active region temperature rises with increased etch depth due to an increased spreading resistance into the substrate.

Comparison of different device mountings

In the previous sections, the investigations have been carried out on a standard ridge waveguide mounted substrate side down. In this configuration heat must escape from the active region through the substrate to the heat sink. Efficient heat transfer in this direction is prevented by the small $\kappa_{\perp}$ in the active region and consequently substantial active region heating occurs. As described in the introduction, alternate device configurations have been used (gold-covered ridges, epilayer down bonding, buried heterostructures mounted epilayer

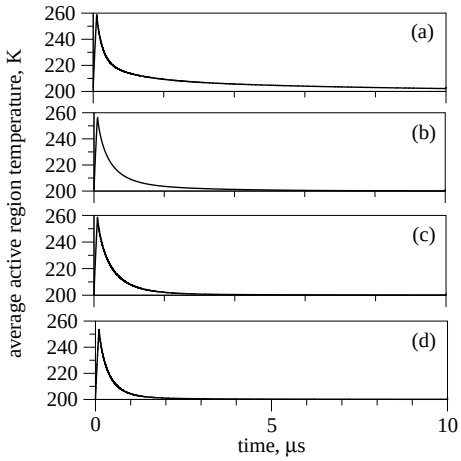

FIG. 5: Temperature–time profiles for (a) a standard ridge waveguide (b) a double channel waveguide mounted substrate side down with a 5 μm thick gold layer deposited on top (c) a double channel waveguide mounted epilayer down on a copper heat sink and (d) buried heterostructure mounted epilayer down on a diamond heat sink.

TABLE II: Results of fitting the cooling phases of each structure (Fig. 5) to a second-order exponential decay function

$T_{\rm AR} = a_0 + a_1 e^{-t/\tau_1} + a_2 e^{-t/\tau_2}$ ($t > 100$ ns)					
Device	a_0	a_1	$\tau_1(\mu s)$	a_2	$\tau_2(\mu s)$
a	203.0	47.5	0.19	32.1	2.67
b	203.1	75.5	0.17	13.7	1.98
c	200.1	32.4	0.14	52.3	0.47
d	200.1	43.7	0.12	45.3	0.33

down) to improve heat dissipation in the active region and in order to compare them, temperature–time profiles and device cross-section temperature profiles were calculated for each. The average active region temperatures as a function of time for the different configurations are shown in Fig. 5. A T_{sink} = 200 K is used with a pulse width of 100 ns at 100 kHz. It can be seen from the figure that at the end of the 100 ns pulse, the ridge waveguide (a) has the highest temperature (262 K) with the gold covered (b) and epilayer down mounted (c) having temperatures of 258 K at the end of the pulse. The BH has the lowest temperature of 252 K. For these driving conditions (in particular the short pulse width), the effect of the different geometries on the active region temperature is relatively small although they do play a large part in the ability of the devices to dissipate the accumulated heat in between the pulses. In order to quantify the ability to dissipate heat, the cooling phases of the temperature–time profiles were fitted using a second-order exponential decay function and the results are summarised in Table II. From the table it can be seen that the substrate side mounted devices (a and b) have higher values of a_0 than the epilayer-down mounted devices due to the heat accumulation effects in these configurations. The second-order exponential fit represents the two distinct cooling phases in the structures, namely the initial escape of heat from the active region and then the diffusing of heat through the substrate and cladding regions to the heat sink. The thermal time constants τ_1 and τ_2 represent these respective cooling stages. Due to the substrate side mounted devices being similar in the fact they have the same cladding and substrate, τ_1 is relatively similar in both structures. The epilayer down mounted devices have smaller values of τ_1 due to the heat sink being in closer proximity to the active region and hence have a steeper temperature gradient between the active region and heat sink that in the substrate side mounted devices. The BH has the smallest τ_1 due to heat being able to escape from the active region both laterally and vertically. As mentioned previously, the active region thermal conductivity in the lateral direction is greater than in the vertical direction and hence the lateral heat channels in the BH offer more efficient heat dissipation than the primarily vertical heat channels in the other devices. From the data is appears that the second stage of cooling represented by τ_2 dominates the cooling phase. Since in the substrate mounted devices, the heat has to diffuse through the entire substrate to the heat sink, the values of τ_2 are much greater in these devices than the epilayer down mounted devices (τ_2 is eight times smaller in the BH than the standard ridge structure). In order to further investigate the effect of the geometry on the heat dissipation capability of the devices, the cross-sectional temperature profiles at t = 1 μs were calculated for each configuration and are shown in Fig. 6. The substrate side mounted devices have similar temperature profiles, with heat primarily escaping through the substrate, although the thick gold layer in device (b) offers and extra heat removal channel from the active region which results in a reduction in the average active region temperature at t = 1 μs from 225 K in the standard ridge to 210 K in the gold covered device. Fig. 6(d) shows the heat escaping from the buried heterostructure active region in all directions compared to the primarily vertical heat channel in the epilayer down mounted double-channel ridge waveguide (Fig. 6(c)), leading to a lower average active region temperature. Table II and Fig. 6 highlight the fact that a buried heterostructure is the best solution in terms of thermal management of QCLs, especially in conjunction with epilayer down mounting. As well as the reduced active region temperature, the temperature profile inside the active region is much more uniform and so the majority of the periods will be at the same temperature. Despite this improvement, the increased performance must be balanced against the much more complicated processing techniques required.

CONCLUSION

To conclude, a QCL thermal model has been presented. The model takes into account temperature dependent material parameters and the anisotropism of the active region thermal conductivity. The power density in the QCL active region was calculated using a self-consistent carrier transport model and then inserted into the developed thermal model to investigate the influence of various driving conditions and device geometry on the QCL active region temperature. Buried heterostructures are found to be the best solution in terms of thermal management due to heat being able to dissipate from the active region in all directions, leading to thermal time constants several

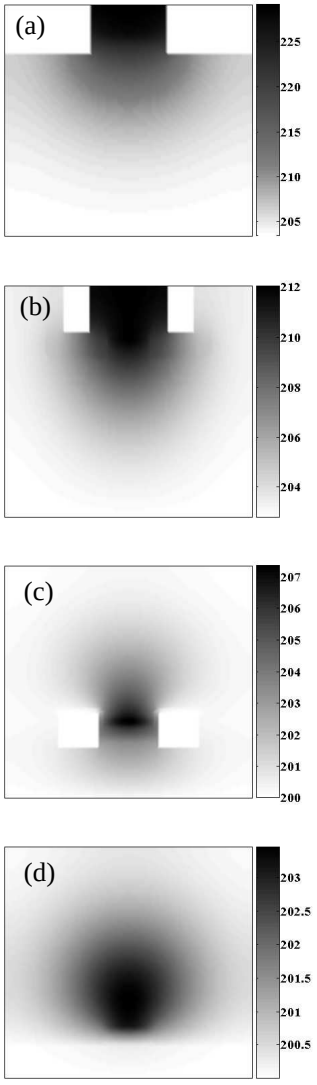

FIG. 6: Cross sectional temperature profiles for each of the devices in Fig. 5, 1 μs into the period (0.99 μs into the cooling stage). Note the different temperature scales.

times smaller than those found in standard ridge waveguides. In this present work, the thermal model was used to investigate the thermal dynamics in a near-infrared InGaAs/AlAsSb QCL but it is equally applicable to all QCL material systems and wavelength ranges. In particular, the thermal model should prove especially useful in the design and optimization of terahertz (THz) QCLs due their sensitivity to temperature due to smaller energy gaps between laser levels and reduced conduction band offsets. It should also be useful in improving the temperature performance in GaAs-based QCLs. Room temperature pulsed mode operation has been reported in the mid-infrared, although to date no report of room temperature cw emission has been made. The fact that GaAs has a lower thermal conductivity than InP means that knowledge of the thermal dynamics inside GaAs-based QCLs must be understood in order to close the gap in temperature performance with InP-based QCLs. A side effect of active region heating is a change in the optical length of the cavity due to a change in refractive index. This reflects in a frequency sweep of the output radiation and this can be controlled by careful engineering of the thermal properties of the device. For example, the thermal model could be used to design a device which gives a constant wavelength shift in time.

Acknowledgment

The authors would like to thank the EPSRC (UK) for financial support.

[1] M. Beck, D. Hofstetter, T. Aellen, J. Faist, U. Oestrele, M. Ilegems, E. Gini, and H. Melchior, "Continuous wave operation of a mid-infrared semiconductor laser at room temperature," *Science*, vol. 295, p. 301–305, 2002.

[2] A. Evans, J. Nguyen, S. Slivken, J. S. Yu, S. R. Darvish, and M. Razeghi, "Quantum-cascade lasers operating in continuous-wave mode above 90 ^{0}C at $\lambda \sim 5.25\mu$m," *Appl. Phys. Lett.*, vol. 88, no. 051105, 2006.

[3] J. S. Yu, S. Slivken, S. R. Darvish, A. Evans, B. Gokden, and M. Razeghi, "High-power, room-temperature, and continuous-wave operation of distributed-feedback quantum-cascade lasers at $\lambda \sim 4.8\mu$m," *Appl. Phys. Lett.*, vol. 87, no. 041104, 2005.

[4] A. Evans, J. S. Yu, J. David, L. Doris, K. Mi, S. Slivken, and M. Razeghi, "High-temperature, high-power, continuous-wave operation of buried heterostructure quantum-cascade lasers," *Appl. Phys. Lett.*, vol. 84, no. 3, p. 314–316, 2004.

[5] J. S. Yu, S. R. Darvish, A. Evans, J. Nguyen, S. Slivken, and M. Razeghi, "Room-temperature continuous-wave operation of quantum-cascade lasers at $\lambda \sim 4\mu$m," *Appl. Phys. Lett.*, vol. 88, no. 041111, 2006.

[6] A. Evans, J. S. Yu, S. Slivken, and M. Razeghi, "Continuous-wave operation of $\lambda \sim 4.8\mu$m quantum-cascade lasers at room temperature," *Appl. Phys. Lett.*, vol. 85, no. 12, p. 2166–2168, 2004.

[7] D. G. Revin, L. R. Wilson, E. A. Zibnik, R. P. Green, and J. W.Cockburn, "InGaAs/AlAsSb quantum cascade lasers," *Appl. Phys. Lett.*, vol. 85, no. 18, p. 3992–3994, 2004.

[8] Q. Yang, C. Manz, W. Bronner, C. Mann, L. Kirste, K. Köhler, and J. Wagner, "GaInAs/AlAsSb quantum-cascade lasers operating up to 400 K," *Appl. Phys. Lett.*, vol. 86, no. 131107, 2005.

[9] Q. Yang, C. Manz, W. Bronner, L. Kirste, K. Köhler, and J. Wagner, "GaInAs/AlGaAsSb quantum-cascade lasers," *Appl. Phys. Lett.*, vol. 86, no. 131109, 2005.

[10] Q. Yang, C. Manz, W. Bronner, R. Moritz, C. Mann, G. Kaufel, K. Köhler, and J. Wagner, "Continuous-wave operation of GaInAs/AlGaAsSb quantum-cascade lasers," *IEEE Photon. Technol. Lett.*, vol. 17, no. 11, p. 2283–2285, 2005.

[11] D. Indjin, P. Harrison, R. W. Kelsall, and Z. Ikonić, "Mechanisms of temperature performance degradation in terahertz quantum-cascade lasers," *Appl. Phys. Lett.*, vol. 82, no. 9, p. 1347–1349, 2003.

[12] V. D. Jovanović, D. Indjin, N. Vukmirović, Z. Ikonić, P. Harrison, E. H. Linfield, H. Page, X. Marcadet, C. Sirtori, C. Worrall, H. E. Beere, and D. A. Ritchie, "Mechanisms of dynamic range limitations in GaAs/AlGaAs quantum cascade lasers: Influence of injector doping," *Appl. Phys. Lett.*, vol. 86, no. 211117, 2005.

[13] C. A. Evans, V. D. Jovanović, D. Indjin, Z. Ikonić, and P. Harrison, "Design and simulation of InGaAs/AlAsSb quantum-cascade lasers for short wavelength emission," *Appl. Phys. Lett.*, vol. 87, no. 141109, 2005.

[14] D. G. Revin, M. J. Steer, L. R. Wilson, R. J. Airey, J. W. Cockburn, E. A. Zibnik, and R. P. Green, "InGaAs-AlAsSb quantum cascade structures emitting at 3.1 μm," *Electron. Lett.*, vol. 40, no. 14, p. 874–875, 2004.

[15] P. Harrison, *Quantum Wells, Wires, and Dots: Theoretical and Computational Physics, 2nd Edition*. Wiley, Chichester, 2005.

[16] E. Anemogiannis, E. N. Glytsis, and T. K. Gaylord, "Determination of Guided and Leaky Modes in Lossless and Lossy Planar Multilayer Optical Waveguides: Reflection Pole Method and Wavevector Density Method," *J. Lightwave Technol.*, vol. 17, no. 5, pp. 929–941, May 1999.

[17] M. Sotoodeh, A. Khalid, and A. Rezazadeh, "Empirical low-field mobility model for III-V compounds applicable in device simulation codes," *J. Appl. Phys.*, vol. 87, no. 6, p. 2890–2900, March 2000.

[18] W. S. Capinski, H. J. Maris, T. Ruf, M. Cardona, K. Ploog, and D. S. Katzer, "Thermal-conductivity measurements of GaAs/AlAs superlattices using a picosecond optical pump-and-probe technique," *Phys. Rev. B*, vol. 59, pp. 8105–8113, 1999.

[19] G. Chen, "Thermal conductivity and ballistic-phonon transport in the cross-plane direction of superlattices," *Phys. Rev. B*, vol. 57, pp. 14 958–14 973, 1998.

[20] C. Pflügl, M. Litzenberger, W. Schrenk, D. Pogany, E. Gornik, and G. Strasser, "Inferometric study of thermal dynamics in GaAs-based quantum-cascade lasers," *Appl. Phys. Lett.*, vol. 82, no. 11, p. 1664-1666, 2003.

[21] Y. G. Zhang, Y. J. He,A. I. Li, "Transient thermal analysis of InAlAs/InGaAs/InP mid-infrared quantum cascade lasers" *Chin. Phys. Lett.*, vol. 20, no. 5, p. 678-681, 2002.

[22] S. T. Huxtable, Ph.D. Thesis, University of California, Berkeley (2002).

[23] C. Gmachl, A. M. Sergent, A. Tredicucci, F. Capasso, A. L. Hutchinson, D. L. Sivco, J. N. Baillargeon, S. N. G. Chu, and A. Y. Cho, "Improved cw operation of quantum cascade lasers with epitaxial-side heat-sinking" *IEEE Photon. Technol. Lett.*, vol. 11, no. 11, p.1369–1371, 1999.

[24] J. S. Yu, A. Evans, S. Slivken, S. R. Darvish, and M. Razeghi, "Short wavelength ($\lambda \sim 4.3\mu m$) high-performance continuous-wave quantum-cascade lasers," *IEEE Photon. Technol. Lett.*, vol. 17, no. 6, p.1154–1156, 2005.

[25] S. Slivken, J. S. Yu, A. Evans, J. David, L. Doris, and M. Razeghi, "Ridge-width dependence on high-temperature continuous-wave quantum-cascade laser operation," *IEEE Photon. Technol. Lett.*, vol. 16, no. 3, p. 744–746, 2004.